Universal strategy towards high–energy aqueous multivalent ion batteries

Xiao Tang
University of Technology Sydney
Dong Zhou
School of Mathematical and Physical Sciences, University of Technology Sydney
https://orcid.org/0000-0002-2578-7124
Bao Zhang
Huazhong University of Science and Technology https://orcid.org/0000-0003-3236-221X
Shijian Wang
University of Technology Sydney
Peng Li
Nanjing University of Aeronautics and Astronautics
Hao Liu
University of Technology Sydney https://orcid.org/0000-0003-0266-9472
Xin Guo
University of Technology Sydney
Pauline Jaumaux
University of Technology Sydney
Xiaochun Gao
University of Technology Sydney
Yongzhu Fu
Zhengzhou University https://orcid.org/0000-0003-3746-9884
Chengyin Wang
College of Chemistry and Chemical Engineering, Yangzhou University, 180 Si-Wang-Ting Road, Yangzhou, 225002, China.
Chunsheng Wang
University of Maryland, College Park https://orcid.org/0000-0002-8626-6381
Guoxiu Wang (Guoxiu.Wang@uts.edu.au)
University of Technology Sydney https://orcid.org/0000-0003-4295-8578

Article

Keywords: non–aqueous rechargeable multivalent metal, energy storage, batteries

Posted Date: January 18th, 2021

DOI: https://doi.org/10.21203/rs.3.rs-140085/v1

Version of Record: A version of this preprint was published at Nature Communications on May 17th, 2021. See the published version at https://doi.org/10.1038/s41467-021-23209-6.

Abstract

Non–aqueous rechargeable multivalent metal (Ca, Mg, Al, *etc.*) batteries are promising for large–scale energy storage due to their low cost. However, their practical applications face formidable challenges owing to low electrochemical reversibility and dendrite growth of multivalent metal anodes, sluggish kinetics of multivalent ion in metal oxide cathodes, and poor electrode compatibility of flammable organic electrolytes. To overcome these intrinsic hurdles, we develop aqueous multivalent ion batteries to replace the prevailing non–aqueous multivalent metal batteries by using wide–window super–concentrated aqueous gel electrolytes, the versatile high–capacity sulfur anodes, and high–voltage metal oxide cathodes. This rationally designed aqueous battery chemistry enables the long–lasting multivalent ion batteries featured with increased high energy density, reversibility and safety. As a demonstration model, a calcium ion–sulfur||metal oxide full cell exhibited a high energy density of 110 Wh kg^{-1} with outstanding cycling stability. Molecular dynamics modelling and experimental investigations revealed that the side reactions could be significantly restrained through the suppressed water activity and formation of protective inorganic solid electrolyte interphase in the aqueous gel electrolyte. The unique redox chemistry has also been successfully extended to aqueous magnesium ion and aluminum ion–sulfur||metal oxide batteries. This work will boost aqueous multivalent ion batteries for low–cost large–scale energy storage.

Introduction

Reliable large–scale energy storage is indispensable for integrating renewable energies (*e.g.* solar and wind) into electric grids[1]. As cost–effective alternatives to lithium (Li) ion batteries, rechargeable multivalent ion batteries (MIBs) are ideal energy storage technologies for grid–scale applications[2]. Among many multivalent cations, Ca^{2+}, Mg^{2+}, and Al^{3+} are of particular interest owing to their non–toxicity, stable valence states, relatively small ionic radii, low redox potentials (Ca/Ca^{2+}: –2.87 V; Mg/Mg^{2+}: –2.36 V; Al/Al^{3+}: –1.68 V *vs.* standard hydrogen electrode (SHE)), and natural abundance (Ca: 4.86 wt%; Mg: 2.60 wt%; Al: 8.21 wt% in earth crust, whereas Li is only 0.0065 wt%)[3,4]. More importantly, such multivalent cations can transfer more than one electron per cation, which can increase energy densities[5].

Despite the above merits, the research progress on MIBs is far from satisfactory. The first challenge is the slow kinetics of multivalent cation insertion/extraction into metal oxide cathodes in organic electrolytes. Metal oxides[6] generally exhibit higher potential and/or capacity than other cathode materials (*e. g.* sulfides[7,8], polyanions[9], Prussian blue analogues[10] and organic compounds[11]), which benefits high energy density. However, the strong electrostatic interactions between multivalent ions and organic solvent molecules as well as cathode host lattices leads to sluggish cation diffusion, which triggers huge polarization and poor cycling stability[12]. Regarding anodes, multivalent cations are difficult to penetrate through the organic component–rich passivating interphase layers on the surfaces of Ca, Mg, and Al metal anodes[13,14], in which the organic components are mainly formed due to the reduction of organic solvents in electrolytes[15]. Only few organic electrolytes using highly flammable ether solvents (*e. g.* tetrahydrofuran[16,17]) can avoid the formation of organic component–rich passivating interphase layers and thus support the reversible plating/stripping of multivalent metal anodes. However, the uncontrollable dendrite growth on the multivalent metal surfaces causes huge safety concern[18]. Furthermore, the low oxidation resistance (<0.9 V *vs.* SHE) of such ether–based electrolytes inhibits the use of high–voltage metal oxide cathodes[19,20]. Other anode materials such as alloys[21,22], carbonaceous materials[23], and polymeric anodes[24] can only deliver limited capacities (generally less than 300 mAh g^{-1}) in MIBs. Therefore, it is essential to re–design battery chemistry for the development of MIBs.

Herein, we re–invent the MIB chemistry by rationally designing high–voltage aqueous batteries. Super–concentrated aqueous gel electrolytes featured with low toxicity and non–flammability were used to replace flammable organic ether–based electrolytes. Such aqueous gel electrolytes have vastly expanded the voltage windows of aqueous electrolytes, and thereby support high–energy–density electrochemical redox couples based on high–voltage metal oxide cathodes (M_xMnO_2, M represents Ca, Mg, and Al). Moreover, the kinetics of multivalent cation insertion/extraction in metal oxide cathodes is extremely fast in aqueous gel electrolytes due to water/proton co–insertion[25]. We chose sulfur as multivalent–ion conversion anode material to avoid the irreversible plating/stripping and dendrite growth of multivalent metal anodes. The high theoretical capacity of sulfur (1675 mAh g^{-1}) is close to those of multivalent metal anodes (Ca, Mg, and Al)[26]. More importantly, the relatively high potential of sulfur in aqueous electrolytes can avoid the formation of organic component–rich interphase layers originated from the reduction of organic solvent, which have been validated in aqueous Li ion–sulfur batteries[27,28]. Conversely, in the super–concentrated aqueous gel electrolytes, a protective inorganic solid electrolyte interphase (SEI) formed on sulfur anode enables a highly reversible anodic polysulfide conversion, which is usually problematic in non–aqueous MIBs. Furthermore, the high–voltage metal oxide cathodes endow the aqueous full batteries with high output voltages comparable to those of non–aqueous MIBs, which ensures to achieve high energy densities. Thus, the aqueous multivalent ion–sulfur||metal oxide batteries revolutionize the less reversible non–aqueous multivalent battery chemistry to completely reversible with high energy, power and high safety; it should be noted that aqueous multivalent ion–sulfur||metal oxide batteries are not an extension of aqueous Li ion–sulfur||metal oxide batteries, which increases the battery safety by scarifying the energy density[29].

As a demonstration model, this aqueous multivalent ion–sulfur||metal oxide chemistry has been successfully deployed in the most challenging Ca–based battery system, where only few cyclable batteries have been previously reported[13,17,29]. The as–developed full aqueous Ca ion–sulfur battery (ACSB) consists of a sulfur@carbon (S@C) anode, a layered $Ca_{0.4}MnO_2$ cathode, and a gel electrolyte based on 8.37 m saturated $Ca(NO_3)_2$ aqueous solution. The low–water–activity of gel electrolyte effectively suppresses the capacity loss caused by calcium polysulfide dissolution in the anode, and simultaneously facilitates a fast and stable calcium ion intercalation/deintercalation in the cathode. The as–developed ACSBs deliver a high energy density of 110 Wh kg^{-1}, 83 % capacity retention after 150 cycles at 0.2 C, and superior safety in the aqueous gel electrolyte. Furthermore, we demonstrate that this strategy can also be extended for building high–energy aqueous Mg ion and Al ion–sulfur||metal oxide batteries.

Results And Discussion

Super–concentrated aqueous gel electrolyte. $Ca(NO_3)_2$ salt was chosen for preparing electrolytes because it has a high solubility (up to 8.37 m) in water comparable to those of fluorinated Ca salts (calcium (II) bis(trifluoromethylsulphonyl)imide ($Ca(TFSI)_2$) and calcium (II) trifluoromethanesulfonate ($Ca(OTf)_2$), *etc.*). Meanwhile, its low cost and eco–friendliness benefit for large–scale applications. It is well known that the electrochemical stability window, imposed by hydrogen evolution reaction (HER) on the anode and oxygen evolution reaction (OER) on the cathode, restricts the application of electrode materials in aqueous batteries. The electrochemical stability window should be wide enough to support the redox couples of the battery chemistry, because even trace amounts of hydrogen or oxygen evolution will seriously deteriorate the cycle life and Coulombic efficiency of batteries[30]. We evaluated the electrochemical stability windows of the aqueous $Ca(NO_3)_2$ electrolytes with different molalities and a gel electrolyte with 10 wt% polyvinyl alcohol (PVA) dissolved in saturated $Ca(NO_3)_2$ aqueous solution by linear sweep voltammetry (LSV) on stainless–steel electrodes. The 1 m $Ca(NO_3)_2$ aqueous electrolyte exhibits weak acidity (Supplementary Fig. 1), and delivers a narrow stability window of only ≈1.75 V (Fig. 1a). The onset potential for HER in electrolytes continually decreases with the increase of $Ca(NO_3)_2$ concentration from –0.6 V *vs.* Ag/AgCl in the 1 m $Ca(NO_3)_2$ electrolyte to –1.1 V in the saturated electrolyte, and further decreases to –1.2 V after adding of PVA, which is far beyond the thermodynamic stability limitation of water (the left panel of Fig. 1a). Such negative shifts of HER could be attributed to the reduction of free water molecules and the protection of SEI on the anode, which ensures a reversible calciation/de–calciation of sulfur to be within the voltage window of the aqueous gel electrolyte (Fig. 1b). Meanwhile, on the cathode side, the onset potential for OER also increases from 1.15 V *vs.* Ag/AgCl in the 1 m $Ca(NO_3)_2$ electrolyte to 1.4 V in the aqueous gel electrolyte (the right panel of Fig. 1a), mainly owing to the suppressed water activity together with an inner Helmholtz layer populated by NO_3^- anions[28]. This envelops the redox potentials of the $Ca_{0.4}MnO_2$ cathode (≈0.2 V *vs.* Ag/AgCl, Fig. 1b). Overall, this result demonstrates that the synergistic effect of super–high salt concentration and PVA successfully expands the electrochemical stability window to 2.6 V to fulfill the electrochemical redox couple of sulfur anode and $Ca_{0.4}MnO_2$ cathode.

The aqueous electrolytes were studied by both molecular dynamics (MD) simulations and experimental investigations. The MD simulations were employed to study the structure evolution of diluted/saturated $Ca(NO_3)_2$ solution and aqueous gel electrolyte (Fig. 2a~c). In 1 m $Ca(NO_3)_2$ solution with a salt–to–water molar ratio (S: W, *i.e.* $Ca(NO_3)_2$: H_2O) of ≈1: 55, individual Ca^{2+} ions are observed to evenly distributed in the solvent, and on average 6.2 water molecules are coordinated with one Ca^{2+} to form a primary solvation sheath (Fig. 2a). Noticeably, only ≈10.9 % of water molecules are coordinated with Ca^{2+} ions, while others interact with each other through hydrogen bonds (Fig. 2d and Supplementary Fig. S2). Such huge amount of free water molecules usually triggers preferential hydrogen evolution, and prevents the reaction between Ca^{2+} and sulfur. Meanwhile, the NO_3^- are scattered randomly among the water molecules without any coordination with Ca^{2+} cations. When the concentration increases to 8.37 m with a S: W of ≈1: 6.6, large amount of Ca^{2+} ions tend to partially share the primary water sheaths with each other, and more water molecules (63.1 %, Fig. 2d and Supplementary Fig. S2) are coordinated with Ca^{2+}, which significantly reduces the activity of water molecules[28]. Moreover, on average three NO_3^- anions are observed in each Ca^{2+} primary solvation sheath (Fig. 2b), resulting in an interfacial chemistry dominated by the NO_3^- reduction. After dissolving PVA into the saturated solution, the Ca^{2+}–H_2O complexes exhibit a polymer–like aggregation (Fig. 2c). This suggests that large amount of water molecules is immobilized by highly concentrated $Ca(NO_3)_2$ salt and polymer chains. Furthermore, as shown in Fig. 2d and Supplementary Fig. S3, the hydrogen bonds of diluted $Ca(NO_3)_2$ solution are ≈1.35 per water molecule, while this value decreases to ≈1.20 with the concentration increasing to 8.37 m. This suggests a reduction of hydrogen bonds at the saturated state due to the high fraction of coordinated water number. In contrast, hydrogen bonds increase to ≈1.25 in the gel electrolyte, which is mainly due to the formation of hydrogen bonds between the hydroxy group in the PVA and water molecules in the Ca^{2+}–H_2O complexes (Fig. 2d). Such perturbation of the water hydrogen bond network by water–PVA interactions can further reduce the activity of water solvent (see the distance change between two nearest water molecules shown in Supplementary Fig. 4)[31], thus effectively enhancing the electrochemical stability and suppressing the diffusion of the polysulfides into water.

Noticeably, the aqueous gel electrolyte shows an ionic conductivity of 9.42 mS cm^{-1} at 25 ^{o}C (Supplementary Fig. 1), which is higher than those of most organic electrolytes[32]. Raman spectroscopy have been performed to study the interplay among ions, water and PVA. Two peaks at ≈717 and 740 cm^{-1} emerge in the aqueous electrolytes with $Ca(NO_3)_2$ concentration higher than 5 m (Fig. 2e, left panel), suggesting the formation of ion pairs (see crystalline $Ca(NO_3)_2·4H_2O$ as the reference in Supplementary Fig. 5)[33]. The O–H stretching vibration modes of water molecules in aqueous electrolytes are presented in the right panel of Fig. 2e. In the 1 m and 2 m dilute $Ca(NO_3)_2$ electrolytes, the O–H stretching vibrations exhibit broad Raman bands consisting of several components, which are attributed to water molecules with different hydrogen–bonding environments in water clusters.[34,35] Both the width and intensity of this band shrink with the increase of the electrolyte concentration, indicating that the Ca^{2+}–H_2O coordination will break the water's hydrogen–bonding structuring. This is well consistent with the red shifts in the ^1H Nuclear magnetic resonance (NMR) spectra (Supplementary Fig. 6) and the density functional theory (DFT) calculation results (Supplementary Fig. 7). The aqueous gel electrolyte showed only a small hump at ≈3500 cm^{-1} in the Raman spectrum, indicating that the water clusters was significantly diminished in this quasi–solid–state electrolyte.

Conversion mechanism and performances of sulfur@carbon composite anode. It is well known that the short–chain polysulfides (S^{2-}~S_4^{2-}) are highly soluble in water[36], which subsequently shuttle between the electrodes and trigger active material loss and interfacial deterioration. Therefore, to improve the electrochemical performances of ACSBs, it is crucial to decrease the solubility of polysulfides in aqueous electrolyte. It is known that a high solubility of polysulfides will increase the concentration gradient between the sulfur electrode|electrolyte interface and the electrolyte bulk phase, thus accelerating the polysulfides' diffusion according to Fick's Law. Therefore, the solubility of polysulfides can be evaluated based on their calculated diffusivity. MD simulations were performed to investigate the diffusion of a typical soluble polysulfide, CaS_4, in different electrolytes (Fig. 3a, Supplementary Fig. 8, and Supplementary Video 1~3). As shown in left panel of Fig. 3a, CaS_4 diffuses quickly in diluted solution within a short time (10 ns), while the diffusion can be significantly suppressed by applying higher salt concentration and PVA chains. Indeed, although the soluble polysulfides can extract water from electrolyte to form anolyte until reaching equilibrium[27], the MD simulations demonstrates the severe aggregation of calcium polysulfides with obvious domain formation in aqueous gel electrolyte. The as–formed mixture of solid and liquefied anolyte is expected to be not miscible with the bulk gel electrolyte. To experimentally verify this, CaS_4 aqueous solution with dark brown color was added onto the surfaces of electrolyte samples. As shown in Fig. 3b, the added CaS_4 immediately diffused into the 1 m $Ca(NO_3)_2$ diluted electrolyte, whose colour turned to yellow in seconds. The saturated $Ca(NO_3)_2$ electrolyte, however, presented a clear segregation interface between the added CaS_4 solution for up to 2 days. Meanwhile, yellow anolyte can be observed to diffuse below the interface, and the segregation interface became blurry after aging for 5 days. In sharp contrast, the aqueous gel electrolyte remained a clear segregation interface after aging for 5 days. This demonstrates that the dissolution of calcium polysulfides is negligible in the gel electrolyte, which is attributed to the suppressed water activity by the super–concentrated salt and PVA.

The S@C was applied as anode material for the ACSBs, since the porous carbon (Supplementary Fig. 9) can enhance the electronic conductivity of sulfur and further inhibit the dissolution of calcium polysulfides into electrolyte[26]. Cyclic voltammetry (CV) was carried out to explore the reaction mechanism of S@C anode in different electrolytes. It is seen that in non–aqueous electrolytes based on organic solvents (such as propylene carbonate (PC) and tetraethylene glycoldimethyl ether (TEGDME)), the CV curves show cathodic peaks at 1.5~0.75 V *vs.* Ca/Ca^{2+}, while almost no peaks are observed in the anodic scan (inset of Fig. 3c). This indicates an irreversible sulfur conversion chemistry in non–aqueous Ca–S batteries. In contrast, in the aqueous gel electrolyte, a gentle current slope starts at ≈0 V *vs.* Ag/AgCl during the initial cathodic scan, suggesting the transformation from sulfur to CaS_x (x = 4~8) species. This is consistent with the *ex situ* Raman spectrum in Supplementary Fig. 10 (see the S_8 (≈151 cm^{-1}) and S_4^{2-}~S_8^{2-} (≈766 cm^{-1}) peaks[26], black curve). Then, a redox peak at −0.55 ~ −0.90 V is observed, which can be assigned to the solid–liquid transition from long–chain polysulfides to short–chain polysulfides such as CaS_4 (see the intensity decreases of the S_8 and S_{4-8}^{2-} peaks together with the appearance of S_4^{2-} peak at ≈255 cm^{-1} in the Raman spectrum[37], red curve in Supplementary Fig. 10).

Meanwhile, CaS and trace amount of $Ca(HS)_2$ can be detected as the final discharge products based on the in–depth X–ray photoelectron spectroscopy (XPS, Supplementary Fig. 11) and ultraviolet–visible spectroscopy (UV–vis, Supplementary Fig. 12) results. The CaS and $Ca(HS)_2$ generate from the reductions of solid calcium polysulfide aggregates (anhydrous) and liquefied calcium polysulfide anolytes (hydrous), respectively. For the anodic scan, a gentle hump from–1 ~ –0.6 V is related to the oxidation of short–chain polysulfides to S_5^{2-} (415 and 495 cm^{-1} in the Raman spectrum) and SO_3^{2-} (612 cm^{-1} in the in the Raman spectrum, see the orange curve in Supplementary Fig. 10). Then, one peak at around –0.6 ~ –0.2 V appears, corresponding to the transformation back to S_8 with small amount of long–chain polysulfides (see the cyan curve in Supplementary Fig. 10). Therefore, the above results clearly elucidate a reversible sulfur conversion chemistry in the super–concentrated aqueous gel electrolyte.

The interfacial properties, including morphology and strength of the SEI layers, have been investigated by high–angle annular dark field (HAADF)–scanning transmission electron microscope (STEM) and atomic force microscope (AFM). As shown in the STEM image, a ≈3 nm SEI was constructed on the S@C electrode surface after a cathodic CV scanning in 8.37 m $Ca(NO_3)_2$ saturated electrolyte (Supplementary Fig. 13b), meanwhile no SEI was observed in the 1 m $Ca(NO_3)_2$ dilute electrolyte (Supplementary Fig. 13a). The SEI layer in aqueous gel electrolyte exhibited an amorphous structure with a thickness of ≈10 nm due to the participation of PVA polymer matrix (inset of Fig. 3d and Supplementary Fig. 13c). Additionally, the surface of SEI layer–coated S@C anode cycled in the aqueous gel electrolyte shows an average Young's modulus of ≈445 MPa, which is much higher than that cycled in the 1 m $Ca(NO_3)_2$ dilute electrolyte (≈165 MPa, Fig. 3d and Supplementary Fig. 14). Such robustness of SEI is expected to maintain its structural integrity against the electrode deformation during cycling.

The interfacial chemistry occurring on the surface of S@C electrode is further revealed through density functional theory (DFT) calculations and in–depth XPS measurement. As discussed above, NO_3^- ions are not coordinated with Ca^{2+} cations in the diluted electrolytes, while on average three NO_3^- anions are coordinated with one Ca^{2+} solvation sheath in the aqueous gel electrolyte (Fig. 2c). Consequently, the reduction potential of NO_3^- is greatly altered by its intimate interaction with Ca^{2+}. Based on the DFT calculation results shown in the Fig. 3e, the $Ca^{2+}(NO_3^-)_3(H_2O)_x$ decomposes below –0.5 V versus Ag/AgCl, which is significantly higher than the reduction potential of an isolated NO_3^- anion at –0.84 V (Supplementary Fig. 15) and the potential of HER. Therefore, the preferential reduction of NO_3^- anions facilitates the formation of SEI layer on the S@C electrode surface to suppress the further anion decomposition. The Ca 2p in–depth XPS spectra of the as–formed SEI on S@C electrode are presented in the Fig. 3f. In Ca $2p_{3/2}$ doublet, the five peaks at 346.1, 346.3, 346.5, 347.3, and 348.4 eV can be assigned to the CaO, Ca_3N_2, Ca–S species (CaS, $Ca(HS)_2$, *etc.*), $CaCO_3$, and $Ca(NO_3)_2$, respectively[38–42]. The peak intensity of $CaCO_3$ decreases, while the intensities of CaO, Ca_3N_2 and Ca–S species increase with increasing sputtering time. This demonstrates that the $CaCO_3$ (formed from the trace dissolved CO_2)

mainly distributes in the SEI outer layer, while the CaO and Ca_3N_2 (formed from the decomposition of NO_3^-) is the main components of the inner layer of the as–formed SEI[10]. Noticeably, these SEI components can only stably exist as solid deposits on the electrode surface in super–concentrated electrolytes, because they would hydrolyze and dissolve quickly in the water media. Such an inorganic SEI is expected to benefit a negative shift of the HER and a further inhibition of the polysulfide dissolution[28].

Structure evolution and performances of $Ca_{0.4}MnO_2$ cathode. The cathode material of the ACSBs, $Ca_{0.4}MnO_2$, was synthesized via a facile *in situ* electrochemical transformation from Mn_3O_4 precursor. The Mn_3O_4 working electrode was assembled into a cell with the saturated $Ca(NO_3)_2$ electrolyte, Pt counter electrode, and Ag/AgCl reference electrode. Then, the cell was cycled in the voltage window of –0.5~1 V *vs.* Ag/AgCl for electrochemical conversion. During the electrochemical oxidation process, Mn^{2+} in the spinel Mn_3O_4 continuously dissolved into the electrolyte accompanying with the oxidation of Mn^{3+} to Mn^{4+}, which resulted in a structure evolution to form layered MnO_2 with rearrangement of Mn [43,44]. Ca^{2+} cations can be intercalated into the MnO_2, thus forming the birnessite $Ca_{0.4}MnO_2$ (the molecular formula is determined based on an overall Ca: Mn atomic ratio of ≈0.4 according to the inductively coupled plasma (ICP) measurement, Table S3) in the subsequent reduction process (Fig. 4a). The STEM analysis was conducted to characterise the cathode material structure. As shown in Fig. 4b and Supplementary Fig. 16a, the Mn_3O_4 particles with an average diameter of ≈50 nm shows a homogeneous structure with typical atom projection arrangement of spinel. Meanwhile, the selected–area electron diffraction (SAED) pattern (the inset in Fig. 4b) illustrates a tetragonal structure in Mn_3O_4 precursor[45]. After *in situ* electrochemical transformation, the $Ca_{0.4}MnO_2$ nanoparticles become porous with blunted edges (Supplementary Fig. 16b). Moreover, a layered structure with an interlayer spacing of ≈6 Å can be observed in the corresponding HAADF–STEM image and SAED pattern (Fig. 4c). The elemental mapping of $Ca_{0.4}MnO_2$ in Supplementary Fig. 17 confirms the Ca^{2+} intercalation in the $Ca_{0.4}MnO_2$. Synchrotron X–ray powder diffraction was performed to further identify the phase and composition of the cathode material. As shown in Fig. 4d and Supplementary Fig. 18, the Mn_3O_4 precursor exhibits a typical spinel structure with space group of I41/amd[46]. After electrochemical oxidation, the MnO_2 as charge product presents new peaks at ≈6.8° and 20° with most of other sharp peaks vanish, which indicates the phase transformation from spinel to birnessite[47]. These newly formed peaks shift towards lower angles in the pattern of $Ca_{0.4}MnO_2$ after the reduction process, demonstrating that intercalation of Ca^{2+} induces variations in the lattice parameter in the layered MnO_2 structure. Moreover, as shown in Mn 3s XPS (Supplementary Fig. 19), the energy separations (ΔE) were measured to be 5.64, 4.55, and 5.10 eV for the Mn_3O_4, birnessite MnO_2, and $Ca_{0.4}MnO_2$ samples, respectively. According to the linear relationship between the chemical valence of Mn and the ΔE value, the average oxidation states of Mn were calculated to be ≈2.5, 3.95, and 3.19 for Mn_3O_4, birnessite MnO_2, and

$Ca_{0.4}MnO_2$ samples, respectively[48,49]. This verifies the electrochemical transformation mechanism to form the $Ca_{0.4}MnO_2$.

Electrochemical measurements were conducted to characterise the performances of the $Ca_{0.4}MnO_2$ cathode. The CV curves in Fig. 4e show a pair of non–sharp redox peaks located at ≈0.2 V, which can be attributed to the reversible intercalation/deintercalation of Ca^{2+} in the layered structure[50]. Based on Dunn's method[51], it can be speculated that the capacity at peak region is dominated by a diffusion–controlled process (Supplementary Fig. 20). The initial CV curves are highly overlapped, indicating that the $Ca_{0.4}MnO_2$ is highly reversible. The $Ca_{0.4}MnO_2$ cathode can deliver high capacities of 210, 170, 135, 116 mAh g^{-1} based on the mass of $Ca_{0.4}MnO_2$ at current densities of 10, 50, 100, and 200 mA g^{-1} (Supplementary Fig. 21a), which are higher than those of the previously reported cathode materials for Ca–based batteries[24]. It should be noted that the $Ca_{0.4}MnO_2$ cathode is non–rechargeable in TEGDME–based electrolyte and delivers low capacities of ≈20 mAh g^{-1} in PC–based electrolytes, mainly due to the low oxidation resistance of ether solvent and the sluggish Ca^{2+} diffusion into the host lattices in carbonate–based electrolyte, respectively (Supplementary Fig. 22). However, according to galvanostatic intermittent titration technique (GITT) (Supplementary Fig. 21b~23) and electrochemical impedance spectroscopy (EIS) (Supplementary Fig. 24) results, the $Ca_{0.4}MnO_2$ cathode exhibits fast Ca^{2+} diffusion kinetics. Such a fast kinetics is attributed to the reversible pre–insertion of protons and water molecules into the lattice of cathode material, which efficiently decreases the Ca^{2+} diffusion barrier and thus improves the kinetics of batteries (Supplementary Fig. 25)[33,50,52].

Electrochemical performances of the aqueous calcium–ion sulfur batteries. To electrochemically evaluate the ACSBs, CR2032 coin cells were assembled with a configuration of the S@C anode, $Ca_{0.4}MnO_2$ cathode, and aqueous gel electrolyte. Fig. 5a shows the CV curves of the ACSB at the initial cycles, in which a pair of redox peaks are mainly attributed to a combination of the reaction as below:

$$5\ Ca_{0.4}MnO_2 + 2\ S = 2\ CaS + 5\ MnO_2 \quad (1)$$

The 1st CV profile shows relatively low repeatability with the following cycles due to an activation process related to the interfacial wettability improvement and SEI formation, *etc.* This is consistent with the pre–activated charge/discharge profile (Supplementary Fig. 26). The subsequent CV curves are overlapped, suggesting that the cathode and anode are highly reversible in the super–concentrated aqueous gel electrolyte. Figure 5b shows the rate performance of the full cells with different electrolytes. We found that the cell cannot be stably cycled in 1 m $Ca(NO_3)_2$ aqueous electrolyte due to the severe HER (Supplementary Fig. 27), and shows low capacity with poor reversibility in organic electrolytes due to the inferior compatibility between both electrodes with such electrolytes (Supplementary Fig. 28). However, by using the aqueous gel electrolyte, the full ACSB delivers capacities of 86, 66, 46, and 35 mAh g^{-1} (based on the mass of total electrodes) at current densities of 0.1 C, 0.2 C, 0.5 C, and 1 C, respectively (Fig. 5c). These are higher than those using saturated $Ca(NO_3)_2$ aqueous electrolyte (81, 58, 36, and 25 mAh g^{-1}, Supplementary Fig. 29). This result indicates that the super–high salt concentration together with the addition of PVA not only enable the expanded electrochemical window to support the S@C||$Ca_{0.4}MnO_2$ electrochemical redox chemistry, but also efficiently suppress the shuttling of calcium polysulfides. Fig. 5d compares the energy densities of various aqueous batteries. The S@C|gel electrolyte|$Ca_{0.4}MnO_2$ ACSB can achieve a high energy density of 110 Wh kg^{-1} (based on the total mass of S@C and $Ca_{0.4}MnO_2$ materials as well as an average mid–value discharge voltage of ≈1.29 V, Fig. 5c). The energy density achieved for ACSB is obviously higher than the previously reported counterparts, including Ca–[24], Li–[53], Na–[54–56], K–[1], Mg–[57,58], and Al–[59] based aqueous batteries. The cycling performances and corresponding Coulombic efficiencies of the ACSBs are presented in Fig. 5e and Supplementary Fig. 30, respectively. The cell with aqueous gel electrolyte exhibits superior cycling stability with 83 % capacity retention after 150 cycles at 0.2 C with an average Coulombic efficiency of 93 %. These values are much higher than those of the cell with saturated $Ca(NO_3)_2$ aqueous electrolyte (65 % and 86 %) due to the immobilization of calcium polysulfides by PVA. S@C|aqueous gel electrolyte|$Ca_{0.4}MnO_2$ pouch cells were also assembled to demonstrate the high safety of the ACSBs (Supplementary Fig. 31). As shown from Fig. 5f and Supplementary Video 4, the fully charged pouch cell did not exhibit short–circuit or burning after corner–cut, and even deliver a constant voltage after immersing the cut cell into water. This intrinsic safety could endow the ACSBs promising for the applications in extreme conditions, *e. g.* aerospace, deep–sea submarine, and other military devices.

In spite of these good electrochemical performances, it should be noted that there is still room to improve the present ACSB chemistry. Even if the $Ca_{0.4}MnO_2$ cathode material applied in our study seems an optimal choice, it actually has not made full use of the wide electrochemical stability window of the aqueous gel electrolyte. Thereby, the advances in exploring new cathode materials with higher capacity and redox potential could further increase the energy density of current ACSBs.

The high–concentrated aqueous gel electrolytes are universal for all aqueous multivalent ion–sulfur chemistry, and provide a new opportunity to develop high energy, safe, and low–cost batteries. The generality of the aqueous gel electrolyte for multivalent ion–sulfur chemistry has been further demonstrated by rechargeable aqueous Mg ion and Al ion–sulfur||metal oxide batteries (Supplementary Fig. 32~34). The aqueous gel electrolytes prepared by dissolving 10 wt% PVA in saturated $Mg(NO_3)_2$ aqueous solution (Supplementary Fig. 32a~b) or in saturated $Al_2(SO_4)_3$ aqueous solution (Supplementary 33a~b) exhibit extended electrolyte stability windows (more than 2.2 V). The M_xMnO_2 (M= Mg or Al) cathodes synthesized via *in situ* electrochemical transformation from Mn_3O_4 show stable multivalent ion intercalation/deintercalation (Supplementary Fig. 32c and 33c), meanwhile the S@C anodes present highly reversible multivalent ion polysulfide conversion in such aqueous gel electrolytes (Supplementary Fig. 32f and 33f). The aqueous Mg ion–sulfur and Al ion–sulfur full cells deliver satisfactory stability during cycling (Supplementary Fig. 32d and 33d), and stable electrolyte|electrode interfaces with small resistances (Supplementary Fig. 32e and 33e). It should be mentioned that even in the organic electrolytes, Ca/Mg/Al ion batteries still suffer from either low reversibility/dendrite growth on metal anodes or low voltage/poor intercalation cathodes. We migrated these challenges by using non–flammable and cheap aqueous electrolytes, which boost the aqueous multivalent ion batteries for low–cost large–scale energy storage.

Conclusions

In summary, we demonstrate that a versatile aqueous multivalent ion–sulfur chemistry can endow the multivalent ion batteries with high energy density, reversibility and safety. By virtue of this chemistry, we developed a room–temperature aqueous Ca ion–sulfur full battery, which was assembled with a sulfur@carbon anode, a $Ca_{0.4}MnO_2$ cathode, and an aqueous gel electrolyte. The synergistic contribution of super–concentrated $Ca(NO_3)_2$ salt and PVA strongly suppresses the water activity in the gel electrolyte, thus providing an expanded electrochemical stability window to support the sulfur–calcium polysulfide conversion chemistry. The sulfur@carbon anode withstands inhibited polysulfides' shuttling owing to the negligible insolubility of polysulfides in the aqueous gel electrolyte and the protection of SEI layer. Meanwhile, the *in situ* electrochemically synthesized $Ca_{0.4}MnO_2$ cathode exhibits highly stable Ca^{2+} intercalation/deintercalation. The as–developed full calcium ion–sulfur battery achieved a high energy density of 110 Wh kg^{-1} with stable cyclability and excellent safety under abuse conditions. Furthermore, this battery design strategy has been successfully extended to rechargeable aqueous Mg and Al–based battery systems. These key findings make a revolutionary step–forward towards the development of aqueous multivalent ion batteries for low–cost energy storage.

Methods

Materials. The 1 m, 2 m, 5 m, and 8.37 m saturated aqueous electrolytes were prepared by dissolving $Ca(NO_3)_2$ (≈99%, Sigma–Aldrich) in deionized water after nitrogen bubbling, respectively. The gel electrolyte was prepared by dissolving 10 wt % PVA (Mw=50000, Sigma–Aldrich) in the saturated $Ca(NO_3)_2$ aqueous electrolyte at 80 ^{o}C under vigorous stirring.

To prepare the S@C composite, the biomass–derived porous carbon as sulfur host was firstly synthesized according to previous report.[60] Then, the S@C material could be obtained by a melt–diffusion strategy, during which a mixture of porous carbon and sulfur powder (99.99%, Sigma–Aldrich) at a weight ratio of 6: 4 was heated at 155 °C for 12 h. The S@C anodes were fabricated by compressing a mixture of the as–prepared S@C composite and poly(vinylidenedifluoride) (PTFE, 5 wt % aqueous solution) binder in a weight ratio of 9:1 on a titanium mesh (200 mesh) followed by vacuum drying at 60 ^{o}C. The areal loading of sulfur was around 1–2 mg cm^{-2} while the electrode area is around 0.385 cm^2.

The cathode precursor, Mn_3O_4, was synthesized as follow. Typically, 2.25 g $MnSO_4$ (≈99%, Sigma–Aldrich) was dissolved in 150 mL deionized water. Liquid ammonium hydroxide was then dropwise added into the solution under magnetic stirring until the pH reached 11. After reacting overnight at room temperature, brown Mn_3O_4 powders were obtained by centrifuging and washing the precipitation. After that, Mn_3O_4, carbon black, and PTFE (5 wt % aqueous solution) were mixed with a weight ratio of 8:1:1, and then pressed onto a stainless–steel mesh (200 mesh). The areal loading of Mn_3O_4 was around 7~9 mg cm^{-2} while the electrode area was around 0.385 cm^2. Subsequently, electrochemical cells were assembled in a glass cell with the as–prepared Mn_3O_4 electrode as working electrode, a saturated Ag/AgCl as reference electrode, a Pt wire as counter electrode, and an 8.37 m $Ca(NO_3)_2$ aqueous electrolyte. The $Ca_{0.4}MnO_2$ electrode was electrochemically prepared by charging–discharging the electrochemical cell within a voltage window of 2.6~4.1 V *vs.* Ca/Ca^{2+} (–0.5~1.0 V *vs.* Ag/AgCl) at a current density of 50 mA g^{-1} for 10 cycles.

Characterisations. Raman spectra were recorded via a Renishaw inVia Raman spectrometer system (Gloucestershire, UK). Nuclear magnetic resonance (NMR) and solid–state NMR measurements were performed on an Agilent 500 MHz Nuclear Magnetic Resonance and Bruker Avance III Nuclear Magnetic Resonance system, respectively. To visually observe the diffusion of calcium polysulfides in electrolyte, 1 m CaS_4 solution was prepared by heating a aqueous suspension of CaO and sulfur powder in stoichiometric ratio at 90 ^{o}C under N_2 bubbling until all the precipitate was dissolved. XPS measurements with depth profiles were conducted on a PHI 5000 VersaProbe II. The thickness values of the depth profiles were estimated from the SiO_2 calibrated sputtering. UV–vis spectra were measured on Agilent Cary 60 UV–Vis Spectrometer. Thermogravimetric analysis (TGA) was performed on a SDT2960 system under a N_2/Ar flow with a rate of 10 ^{o}C min^{-1}. The pore volume was measured via the Brunauer–Emmett–Teller (BET) method by Micromeritics 3Flex analyzer at 77 K with N_2 as analysis gas. The phase information was collected by synchrotron X–ray powder diffraction with a Cu Kα X–ray source at a scan rate of 1^{o} min^{-1} (operating voltage of 40 kV and current of 25 mA). The FTIR were collected by using Nicolet Magna 6700 FTIR spectrometer. The molecular formulas were determined by ICP–OES (PerkinElmer Optima, PerkinElmer Avio). The morphologies of the samples were probed by using field emission scanning electron microscope (FE–SEM, Zeiss Supra 55VP), and HAADF–STEM (JEOL JEM–ARM200) operated at an accelerating voltage of 200 kV.

Electrochemical measurements. The ionic conductivities of the electrolyte samples were measured by EIS from 10^5 to 1 Hz with an alternating current amplitude of 5 mV at 25 ^{o}C. The test cells were fabricated by soaking two stainless steel mesh in the electrolyte samples. The electrochemical stability window of electrolytes was evaluated by LSV via three–electrode devices assembled with stainless steel mesh as working electrode, saturated silver/silver chloride (Ag/AgCl) as reference electrode, and Pt wire as counter electrode at scan rate of 1 mV s^{-1}. Electrochemical cells were assembled via three electrode configurations with either S@C or $Ca_{0.4}MnO_2$ as working electrode, a saturated Ag/AgCl as reference electrode, and Pt wire as counter electrode. For galvanostatic intermittent titration technique (GITT) measurements, the electrodes were charged/discharged for 10 min at a current density of 50 mA g^{-1}, followed by a duration of 1 h relaxation to achieve equilibrium potential in such three–electrode device. All above electrochemical measures were conducted on a VMP3 multichannel electrochemical station (Bio Logic Science Instruments, France).

For the full cell tests, CR2032 coin cells were assembled with S@C anode, $Ca_{0.4}MnO_2$ cathode, two glass fiber membrane (Whatman GF/A) as separators, and gel electrolyte. The weight ratio of $Ca_{0.4}MnO_2$ to S@C was around 1.6: 1. Prior to cell assembly, electrodes and the separator were soaked with the hot gel, and then aged at room temperature to reach thermal equilibrium. Galvanostatic charge–discharge measurements were performed on a Neware battery test system. Before the cycling and rate tests, the as–developed full cells were first activated by cycling at 0.1~2 V at 0.5 C for 1 cycle (1 C = 1675 mA g^{-1} based on the mass of sulfur) at room temperature. CV of the assembled cells were tested using the VMP3 electrochemical workstation at a scanning rate of 0.2 mV s^{-1}. EISs of cells were examined using the VMP3 multichannel electrochemical station in a frequency range of 10^{-2} to 10^5 Hz by applying a disturbance amplitude of 5 mV.

Computation. Molecular dynamics (MD) simulations were performed to investigate the structures of aqueous solutions/gel electrolyte and the diffusion of polysulfides as a function of salt concentration. The MD simulations were run using LAMMPS[61]. The systems are setup initially by using PACKMOL[62] and Moltemplate (http://www.moltemplate.org/). Periodic boxes were used here. The properties of H_2O are assessed with SPC/E parameters. The force–fields parameters of Ca^{2+} and NO_3^- are taken from previous publications[63,64] with partial charges. The force–fields parameters of PVA chains and polysulfides are taken from OPLS–AA parameters OPLS–AA parameters and previously publications[65]. Herein, an oligomer ($CH_3[C_2H_4O]_4$) form was utilized to simplify the gel electrolyte simulations. A LJ cutoff of 10 Å and a particle–particle particle–mesh solver[66] for long–range Coulombic interactions were also employed.

Density functional theory (DFT) calculations were employed to study the reduction potentials of $Ca^{2+}(NO_3^-)_3(H_2O)_x$ complex and isolated NO_3^- as well as the binding energy. The calculations of reduction potentials and binding energy were performed with Gaussian 16 package[66]. All calculations were carried out with a solvation correction under SMD model[67]. All the thermal dynamic results were obtained with a combined method of G4(MP2)[68], and the final results were corrected as 298 K. The reduction potentials $E(NO_3^-/NO_2^-)$ *vs.* the SHE were calculated according to the reported method[69] from the half reactions:

$$NO_3^- + 2e^- \rightarrow NO_2^- + O^{2-} \quad \Delta G \tag{2}$$

and

$$H^+ + e^- \rightarrow 1/2H_2 \quad \Delta G_{SHE} \tag{3}$$

in which NO_3^- and NO_2^- are the oxidized and reduced iron species in the reduction, and ΔG and ΔG_{SHE} are the aqueous free energy changes for the respective half reactions, ignoring the electron. The final reduction potential (*vs.* SHE) was calculated with the following equation:

$$E = -\left(\frac{\Delta G}{zF} - \frac{\Delta G_{SHE}}{F}\right) \quad (4)$$

where in the reaction, *z* is the charge transfer and F is Faraday constant. The binding energies were calculated using wB97xd functionals[70] with the basis sets of def2–TZVPP[71].

Declarations

Data availability. The data that support the findings of this study are available from the corresponding author upon reasonable request.

Acknowledgements

We would like to acknowledge the support by Rail Manufactory CRC projects (RMCRC: R1.1.1 and R1.1.2), and the Australian Research Council (ARC) Discovery Projects (DP170100436 and DP200101249).

Author contributions

C.W and G.W. conceived and designed this work. D.Z. and X.T. performed the experiments and wrote the manuscript. B.Z. conducted the molecular dynamics simulations. P.L. performed the density functional theoretical calculations. S.W., H.L., X.G., P.J., X.G., Y.F., and C.W. discussed the results and participated in the preparation of the paper.

Additional information

Supplementary information accompanies this paper at http://

Competing financial interests: The authors declare no competing interests.

References

1 Jiang, L. *et al.* Building aqueous K–ion batteries for energy storage. *Nat. Energy* **4**, 495–503 (2019).

2 Son, S.–B. *et al.* An artificial interphase enables reversible magnesium chemistry in carbonate electrolytes. *Nat. Chem.* **10**, 532–539 (2018).

3 Arroyo–de Dompablo, M. E., Ponrouch, A., Johansson, P. & Palacín, M. R. Achievements, challenges, and prospects of calcium batteries. *Chem. Rev.* (2019).

4 Yang, H. *et al.* The rechargeable aluminum battery: opportunities and challenges. *Angew. Chem. Int. Ed.* **58**, 11978–11996 (2019).

5 Li, M. *et al.* Design strategies for nonaqueous multivalent–ion and monovalent–ion battery anodes. *Nat. Rev. Mater.* 1–19 (2020).

6 Liu, Y. *et al.* Layered P2–$Na_{2/3}[Ni_{1/3}Mn_{2/3}]O_2$ as high–voltage cathode for sodium–ion batteries: the capacity decay mechanism and Al_2O_3 surface modification. *Nano Energy* **27**, 27–34 (2016).

7 Geng, L., Lv, G., Xing, X. & Guo, J. Reversible electrochemical intercalation of aluminum in Mo_6S_8. *Chem. Mater.* **27**, 4926–4929 (2015).

8 Aurbach, D. *et al.* Prototype systems for rechargeable magnesium batteries. *Nature* **407**, 724–727 (2000).

9 Mao, M., Gao, T., Hou, S. & Wang, C. A critical review of cathodes for rechargeable Mg batteries. *Chem. Soc. Rev.* **47**, 8804–8841 (2018).

10 Gummow, R. J., Vamvounis, G., Kannan, M. B. & He, Y. Calcium-ion batteries: Current state-of-the-art and future perspectives. *Adv. Mater.* **30**, 1801702 (2018).

11 Pan, B. *et al.* Polyanthraquinone-based organic cathode for high-performance rechargeable magnesium-ion batteries. *Adv. Energy Mater.* **6**, 1600140 (2016).

12 Guduru, R. K. & Icaza, J. C. A brief review on multivalent intercalation batteries with aqueous electrolytes. *Nanomaterials* **6**, 41 (2016).

13 Ponrouch, A., Frontera, C., Bardé, F. & Palacín, M. R. Towards a calcium–based rechargeable battery. *Nat. Mater.* **15**, 169–172 (2016).

14 Attias, R., Salama, M., Hirsch, B., Goffer, Y. & Aurbach, D. Anode–electrolyte interfaces in secondary magnesium batteries. *Joule* **3**, 27–52 (2019).

15 Fan, X. *et al.* All–temperature batteries enabled by fluorinated electrolytes with non–polar solvents. *Nat. Energy* **4**, 882–890 (2019).

16 Chen, J. *et al.* Electrolyte design for LiF–rich solid–electrolyte interfaces to enable high–performance microsized alloy anodes for batteries. *Nat. Energy* **5**, 386–397 (2020).

17 Wang, D. *et al.* Plating and stripping calcium in an organic electrolyte. *Nat. Mater.* **17**, 16–20 (2018).

18 Davidson, R. *et al.* Formation of magnesium dendrites during electrodeposition. *ACS Energy Lett.* **4**, 375–376 (2018).

19 Sun, Y., Zou, Q. & Lu, Y. C. Fast and reversible four–electron storage enabled by ethyl viologen for rechargeable magnesium batteries. *Adv. Energy Mater.* **9**, 1903002 (2019).

20 Mizrahi, O. *et al.* Electrolyte solutions with a wide electrochemical window for rechargeable magnesium batteries. *J. Electrochem. Soc.* **155**, A103 (2007).

21 Wu, N. *et al.* A calcium-ion hybrid energy storage device with high capacity and long cycling life under room temperature. *Adv. Energy Mater.* **9**, 1803865 (2019).

22 Shao, Y. *et al.* Highly reversible Mg insertion in nanostructured Bi for Mg ion batteries. *Nano Lett.***14**, 255–260 (2014).

23 Wu, S., Zhang, F. & Tang, Y. A novel calcium-ion battery based on dual-carbon configuration with high working voltage and long cycling life. *Adv. Sci.* **5**, 1701082 (2018).

24 Gheytani, S. *et al.* An aqueous Ca-ion battery. *Adv. Sci.* **4**, 1700465 (2017).

25 Wang, F. *et al.* How water accelerates bivalent ion diffusion at the electrolyte/electrode interface. *Angew. Chem. Int. Ed.* **57**, 11978–11981 (2018).

26 Xu, X. *et al.* A room–temperature sodium–sulfur battery with high capacity and stable cycling performance. *Nat. Commun.* **9**, 1–12 (2018).

27 Yang, C. *et al.* Unique aqueous Li–ion/sulfur chemistry with high energy density and reversibility. *P. Natl. Acad. Sci.* **114**, 6197–6202 (2017).

28 Suo, L. *et al.* "Water–in–salt" electrolyte enables high–voltage aqueous lithium–ion chemistries. *Science* **350**, 938–943 (2015).

29 Wang, M. *et al.* Reversible calcium alloying enables a practical room–temperature rechargeable calcium–ion battery with a high discharge voltage. *Nat. Chem.* **10**, 667–672 (2018).

30 Borodin, O., Self, J., Persson, K. A., Wang, C. & Xu, K. Uncharted waters: Super–concentrated electrolytes. *Joule* **4**, 69–100 (2020).

31 Xie, J., Liang, Z. & Lu, Y.–C. Molecular crowding electrolytes for high–voltage aqueous batteries. *Nat. Mater.* 1–6 (2020).

32 Liu, Z. *et al.* Voltage issue of aqueous rechargeable metal–ion batteries. *Chem. Soc. Rev.***49**, 180–232 (2020).

33 Tang, I. & Fung, K. Hydration and Raman scattering studies of levitated microparticles: Ba $(NO_3)_2$, $Sr(NO_3)_2$, and $Ca(NO_3)_2$. *J. Chem. Phys.* **106**, 1653–1660 (1997).

34 Auer, B., Kumar, R., Schmidt, J. & Skinner, J. Hydrogen bonding and Raman, IR, and 2D–IR spectroscopy of dilute HOD in liquid D_2O. *P. Natl. Acad. Sci.* **104**, 14215–14220 (2007).

35 Auer, B. & Skinner, J. IR and Raman spectra of liquid water: Theory and interpretation. *J. Chem. Phys.* **128**, 224511 (2008).

36 Yun, S. *et al.* Materials and device constructions for aqueous lithium–sulfur batteries. *Adv. Func. Mater.* **28**, 1707593 (2018).

37 Khan, S. A., Hughes, R. W. & Reynolds, P. A. Raman spectroscopic determination of oxoanions in aqueous polysulfide electrolyte solutions. *Vib. Spectrosc.* **56**, 241-244 (2011).

38 Seyama, H. & Soma, M. X–ray photoelectron spectroscopic study of montmorillonite containing exchangeable divalent cations. *J. Chem. Soc. Faraday Trans.* **80**, 237–248 (1984).

39 Franzen, H. *et al.* XPS spectra and crystalline potentials in alkaline–earth chalcogenides and hydrides. *J. Electron. Spectros. Relat. Phenomena* **11**, 439–443 (1977).

40 Christie, A., Lee, J., Sutherland, I. & Walls, J. An XPS study of ion–induced compositional changes with group II and group IV compounds. *Appl. Surf. Sci.* **15**, 224–237 (1983).

41 Demri, B. & Muster, D. XPS study of some calcium compounds. *J. Mater. Process. Technol.* **55**, 311–314 (1995).

42 Druffel, D. L. *et al.* Experimental demonstration of an electride as a 2D material. *J. Am. Chem. Soc.* **138**, 16089–16094 (2016).

43 Kim, S. *et al.* Direct observation of an anomalous spine-to-layered phase transition mediated by crystal water intercalation. *Angew. Chem. Int. Ed.* **54**, 15094–15099 (2015).

44 Xia, H. *et al.* A monoclinic polymorph of sodium birnessite for ultrafast and ultrastable sodium ion storage. *Nat. Commun.* **9**, 1–10 (2018).

45 San, X., Zhang, B., Wang, J., Wu, B. & Ma, X. Tracking the structural evolution at atomic–scale in the spinel Mn_3O_4 induced by electrochemical cycling. *Electrochem. Commun.* **72**, 166–170 (2016).

46 Jiang, H. *et al.* An aqueous dual-ion battery cathode of Mn_3O_4 via reversible insertion of nitrate. *Angew. Chem. Int. Ed.* **58**, 5286–5291 (2019).

47 Wu, C. *et al.* Electrochemically activated spinel manganese oxide for rechargeable aqueous aluminum battery. *Nat. Commun.* **10**, 1–10 (2019).

48 Beyreuther, E., Grafström, S., Eng, L. M., Thiele, C. & Dörr, K. XPS investigation of Mn valence in lanthanum manganite thin films under variation of oxygen content. *Phys. Rev. B* **73**, 155425 (2006).

49 Lin, B. *et al.* Birnessite nanosheet arrays with high K content as a high-capacity and ultrastable cathode for K-ion batteries. *Adv. Mater,* **31**, 1900060 (2019).

50 Hyoung, J., Heo, J. W. & Hong, S.–T. Investigation of electrochemical calcium–ion energy storage mechanism in potassium birnessite. *J. Power Sources* **390**, 127–133 (2018).

51 Brezesinski, T., Wang, J., Tolbert, S. H. & Dunn, B. Ordered mesoporous α–MoO_3 with iso–oriented nanocrystalline walls for thin–film pseudocapacitors. *Nat. Mater.* **9**, 146–151 (2010).

52 Park, M. J., Yaghoobnejad Asl, H. & Manthiram, A. Multivalent–ion versus proton insertion into battery electrodes. *ACS Energy Lett.* **5**, 2367–2375 (2020).

53 Luo, J.–Y., Cui, W.–J., He, P. & Xia, Y.–Y. Raising the cycling stability of aqueous lithium–ion batteries by eliminating oxygen in the electrolyte. *Nat. Chem.* **2**, 760–765 (2010).

54 Wu, X. y. *et al.* Energetic Aqueous Rechargeable Sodium-Ion Battery Based on $Na_2CuFe(CN)_6$–$NaTi_2(PO_4)_3$ Intercalation Chemistry. *ChemSusChem* **7**, 407–411 (2014).

55 Pasta, M. *et al.* Full open–framework batteries for stationary energy storage. *Nat. Commun.* **5**, 1–9 (2014).

56 Hou, Z., Li, X., Liang, J., Zhu, Y. & Qian, Y. An aqueous rechargeable sodium ion battery based on a $NaMnO_2$–$NaTi_2(PO_4)_3$ hybrid system for stationary energy storage. *J. Mater. Chem. A* **3**, 1400–1404 (2015).

57 Chen, L. *et al.* Aqueous Mg–ion battery based on polyimide anode and Prussian blue cathode. *ACS Energy Lett.* **2**, 1115–1121 (2017).

58 Wang, F. *et al.* High–voltage aqueous magnesium ion batteries. *ACS Cent. Sci.* **3**, 1121–1128 (2017).

59 Wang, P. *et al.* A flexible aqueous Al ion rechargeable full battery. *Chem. Eng. J.* **373**, 580–586 (2019).

60 Tang, X. *et al.* A novel lithium–ion hybrid capacitor based on an aerogel–like MXene wrapped Fe_2O_3 nanosphere anode and a 3D nitrogen sulphur dual–doped porous carbon cathode. *Mater. Chem. Front.* **2**, 1811–1821 (2018).

61 Plimpton, S. Computational limits of classical molecular dynamics simulations. *J. Comput. Phys.* **117**, 361–364 (1995).

62 Martínez, L., Andrade, R., Birgin, E. G. & Martínez, J. M. PACKMOL: a package for building initial configurations for molecular dynamics simulations. *J. Comp. Chem.* **30**, 2157–2164 (2009).

63 Zheng, J. *et al.* Understanding thermodynamic and kinetic contributions in expanding the stability window of aqueous electrolytes. *Chem* **4**, 2872–2882 (2018).

64 Kohagen, M., Mason, P. E. & Jungwirth, P. Accurate description of calcium solvation in concentrated aqueous solutions. *J. Phys. Chem. B* **118**, 7902–7909 (2014).

65 Jorgensen, W. L., Maxwell, D. S. & Tirado–Rives, J. Development and testing of the OPLS all–atom force field on conformational energetics and properties of organic liquids. *J. Am. Chem. Soc.* **118**, 11225–11236 (1996).

66 Hockney, R. W. & Eastwood, J. W. *Computer simulation using particles*. (crc Press, 1988).

67 Marenich, A. V., Cramer, C. J. & Truhlar, D. G. Universal solvation model based on solute electron density and on a continuum model of the solvent defined by the bulk dielectric constant and atomic surface tensions. *J. Phys. Chem. B* **113**, 6378–6396 (2009).

68 Curtiss, L. A., Redfern, P. C. & Raghavachari, K. Gaussian–4 theory. *J. Chem. Phys.* **126**, 084108 (2007).

69 Ali–Torres, J., Rodriguez–Santiago, L., Sodupe, M. & Rauk, A. Structures and stabilities of $Fe^{2+}/^{3+}$ complexes relevant to Alzheimer's disease: an ab initio study. *J. Phys. Chem. A* **115**, 12523–12530 (2011).

70 Chai, J.–D. & Head–Gordon, M. Long–range corrected hybrid density functionals with damped atom–atom dispersion corrections. *Phys. Chem. Chem. Phys.* **10**, 6615–6620 (2008).

71 Weigend, F., Furche, F. & Ahlrichs, R. Gaussian basis sets of quadruple zeta valence quality for atoms H–Kr. *J. Chem. Phys.* **119**, 12753–12762 (2003).

Figures

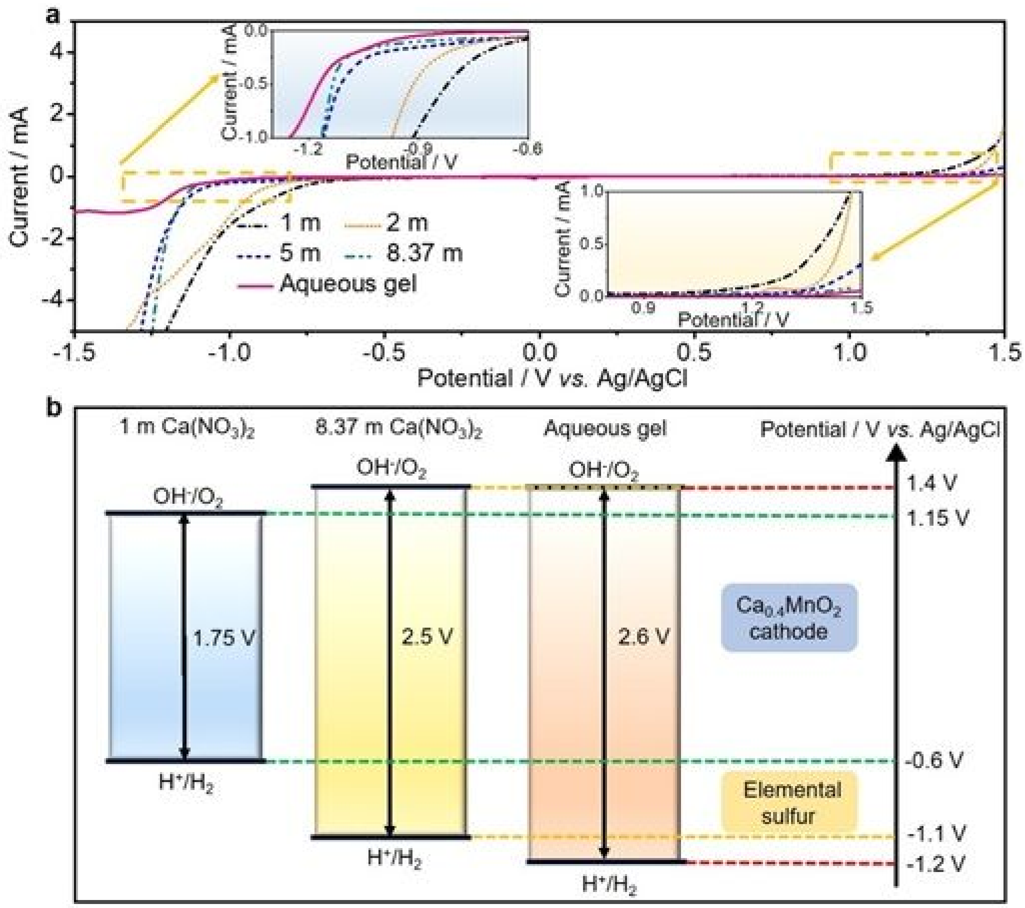

Figure 1

The electrochemical stability window of electrolytes. a Linear voltammetry curves recorded at 1 mV s−1 in 1 m, 2 m, 5 m, saturated (8.37 m) Ca(NO3)2 electrolytes and aqueous gel electrolyte. The insets are the magnified views of the regions marked near anodic and cathodic extremes. b The electrochemical stability windows of electrolytes, and the redox voltages of Ca0.4MnO2 cathode and sulfur anode obtained from experimental data.

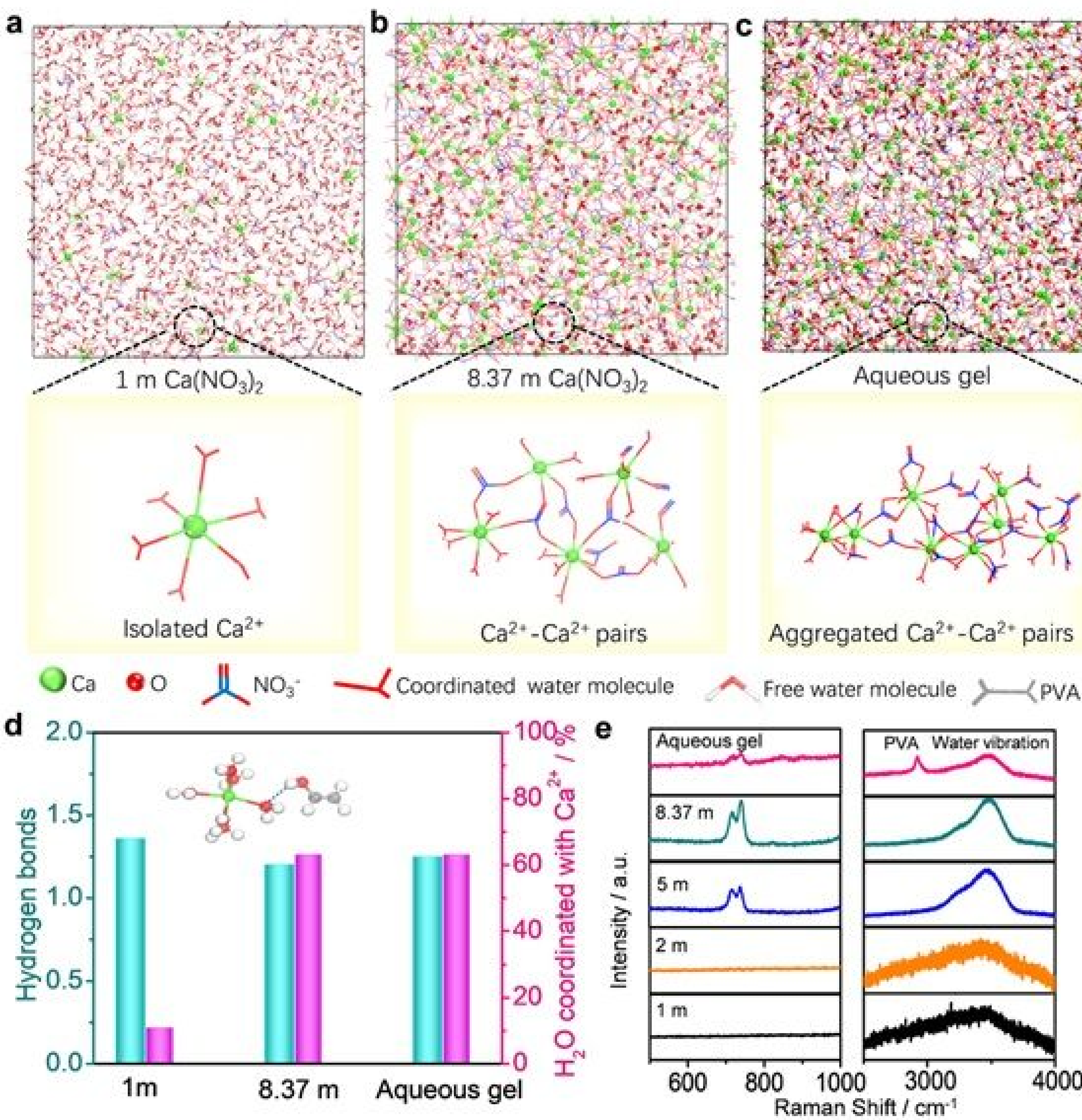

Figure 2

Molecular dynamics simulations and characterisation of electrolytes. Snapshots of local structure evolution for a 1 m Ca(NO3)2 electrolyte, b saturated Ca(NO3)2 electrolyte, and c aqueous gel electrolyte based on MD simulation at 10 ns. d The hydrogen bonds and the percentage of water molecular coordinated with Ca2+ for three electrolyte samples based on MD simulation at 10 ns. The hydrogen bond between the Ca2+–H2O complex and PVA repetitive unit is shown in the inset. The green, red, white and grey balls represent Ca, O, H and C, respectively. e Raman spectra of the 1 m, 2 m, 5 m and saturated Ca(NO3)2 aqueous electrolytes, and aqueous gel electrolyte.

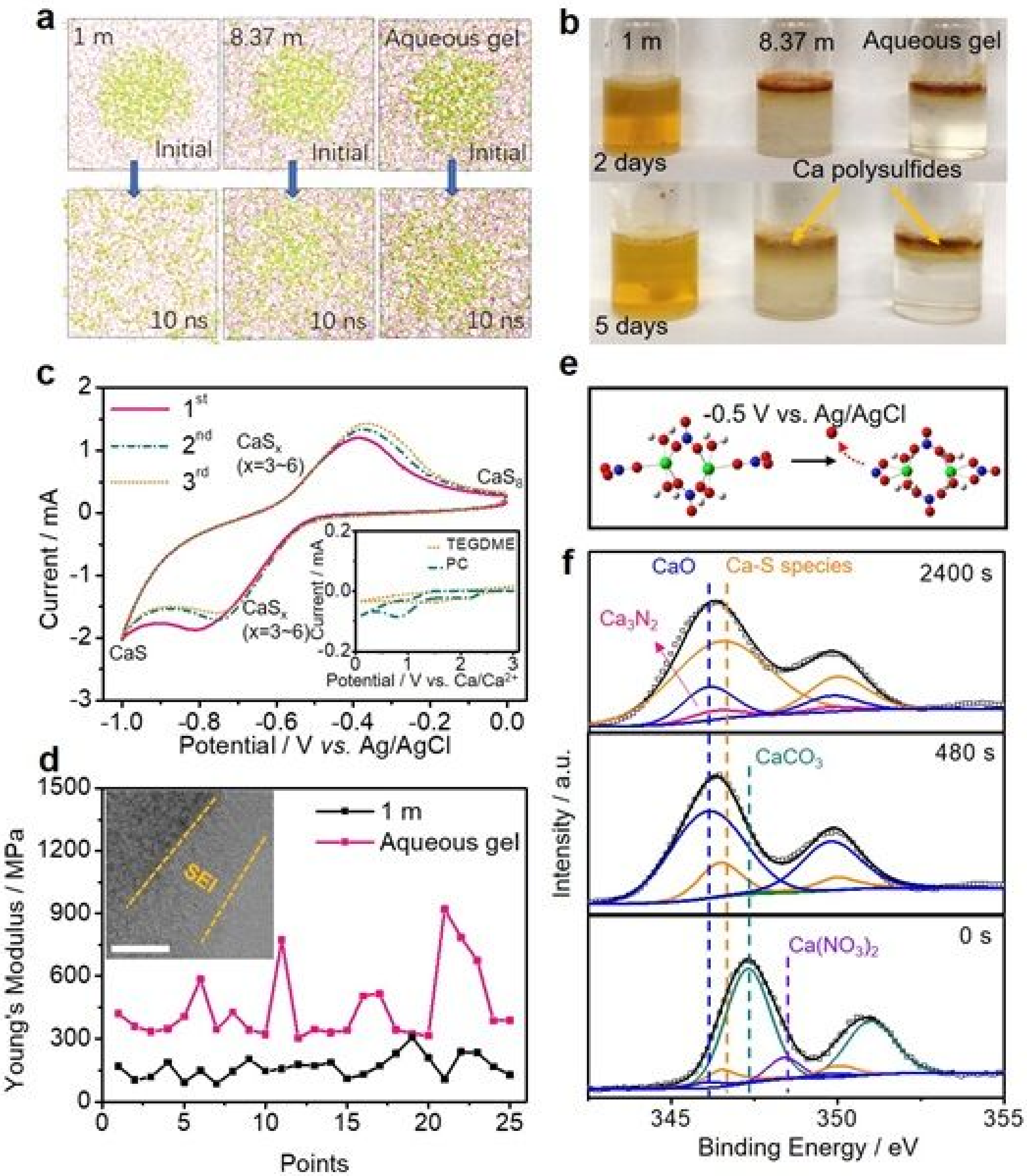

Figure 3

Reaction mechanism of elemental sulfur in the aqueous gel electrolyte. a Local structure evolutions of CaS4 (yellow) diffusions in 1 m, 8.37 m Ca(NO3)2 electrolytes, and aqueous gel electrolyte based on MD simulation. The yellow balls represent S atoms, and other symbols are same with those in Fig. 2a~c. b Visual observation of calcium polysulfides diffusion in 1 m, 8.37 m Ca(NO3)2 electrolyte, and gel electrolyte. c The 1st CV curve of S@C electrode collected at a scan rate of 0.2 mV s−1 in the aqueous gel electrolyte. The CV curves of Ca metal||S@C cell with 0.5 m Ca(OTf)2 in TEGDME or 0.5 m Ca(OTf)2 in PC electrolytes at 0.2 mV s−1 are shown in inset of Fig. 3c. d The Young's Modulus of S@C anodes tested in 1 m Ca(NO3)2 and aqueous gel electrolytes. The points are selected from the AFM scanning images in Supplementary Fig. 12. The inset is HADDF−STEM images of S@C anodes after cycling in aqueous gel electrolyte, scale bar: 10 nm. e The DFT calculations of reduction of Ca2+(NO3−)3(H2O)x aggregate. The green, blue, red and white balls represent Ca, N, O, and H atoms, respectively. f In−depth Ca 2p XPS of the S@C electrode after cathodic CV scanning.

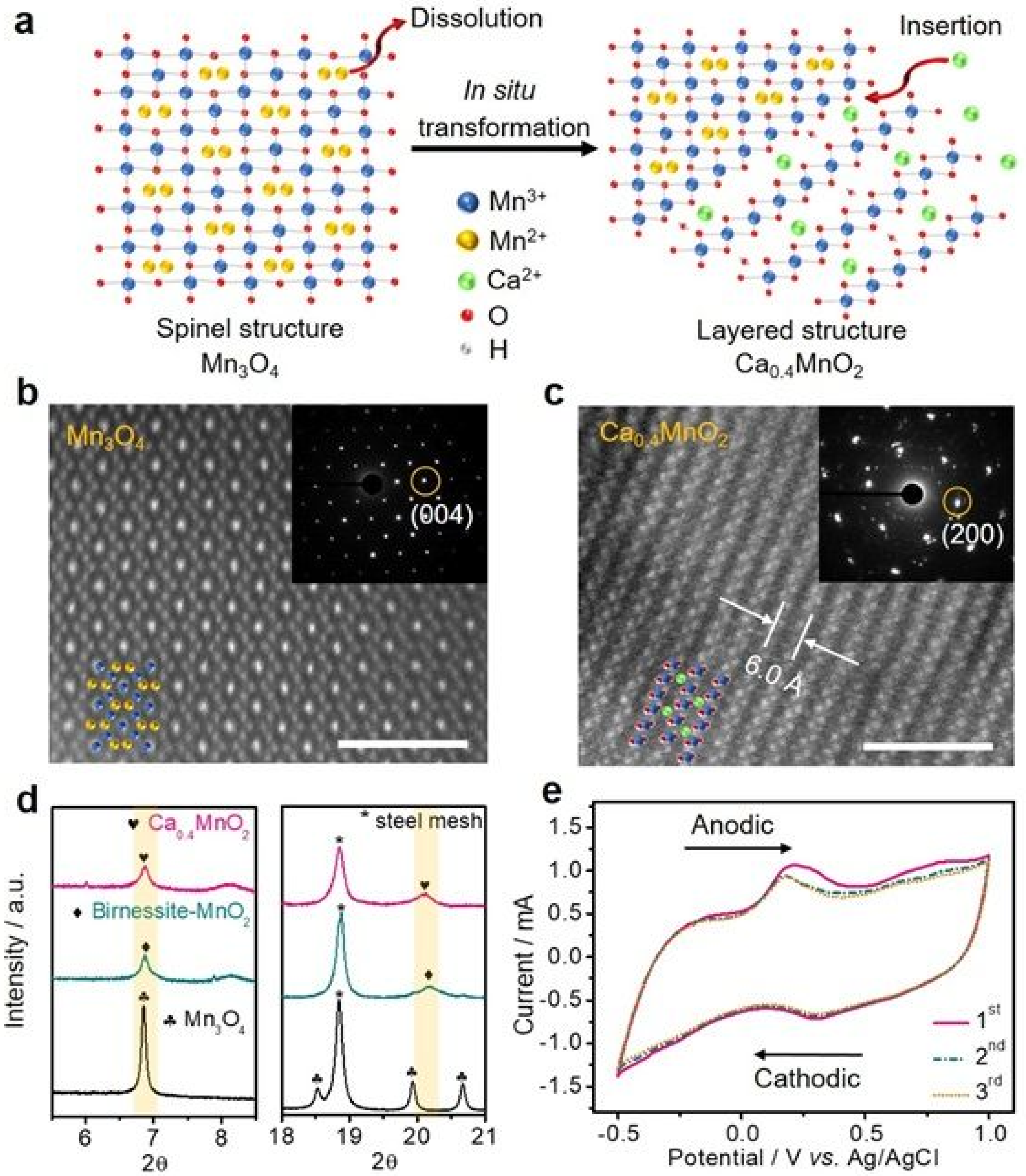

Figure 4

Characterisation of the Ca0.4MnO2 cathode. a Schematic illustration of the atomic structure change during the in situ electrochemical conversion. The HADDF–STEM images of b the Mn3O4 precursor and c The Ca0.4MnO2 cathode material. Blue, orange, green, and red balls represent Mn3+, Mn2+, Ca, and O atoms, respectively. Scale bars are 2 nm in Fig. 4b and c. d Synchrotron powder diffraction patterns of the Mn3O4, birnessite MnO2 and Ca0.4MnO2. The peaks marked with star symbol correspond to the stainless–steel mesh current collector. e CV curves of the Ca0.4MnO2 cathode collected at a scan rate of 0.3 mV s−1.

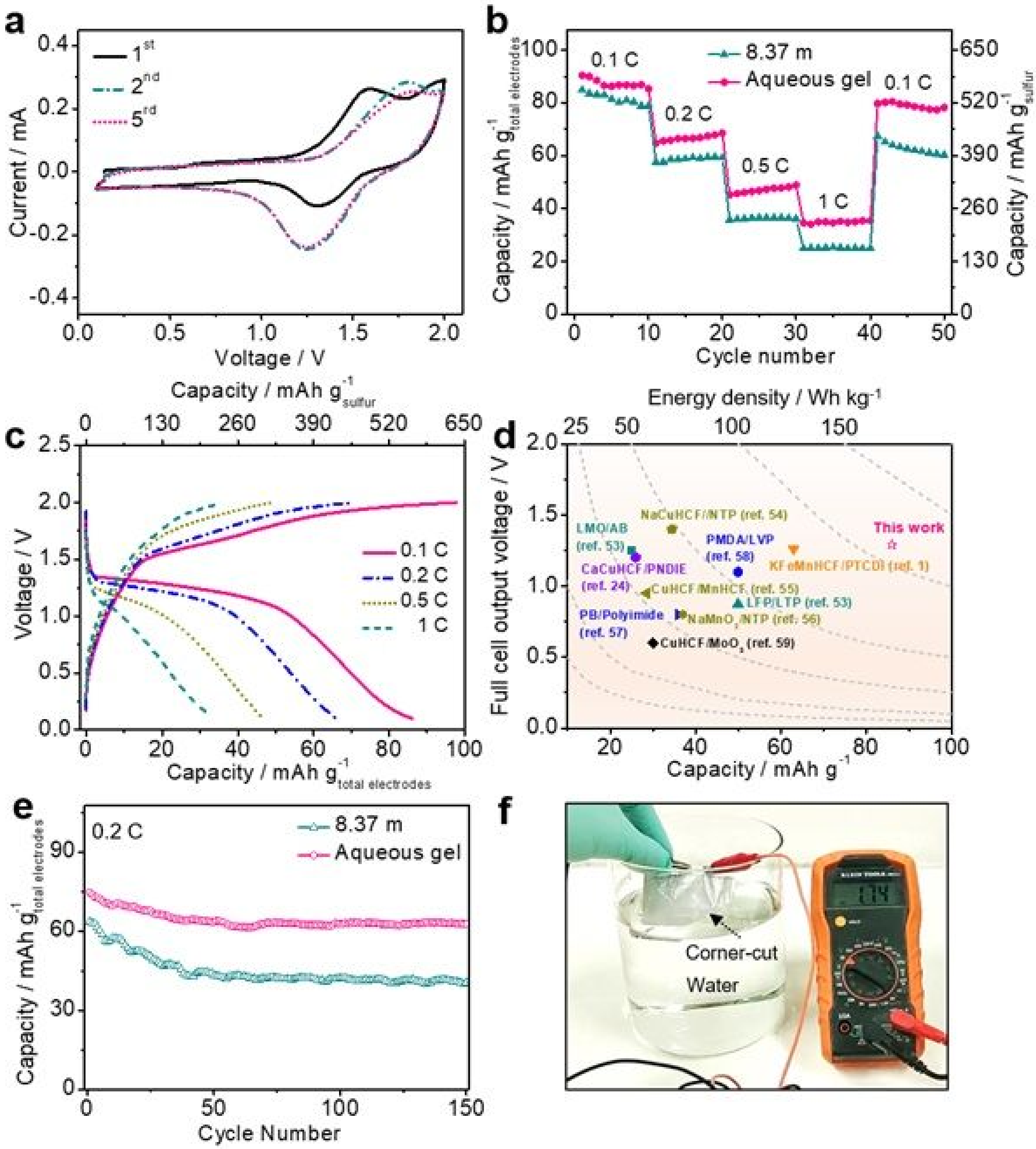

Figure 5

The electrochemical performances of the as−assembled ACSBs. a The CV curves of the S@C|aqueous gel electrolyte|Ca0.4MnO2 full cell collected at a scan rate of 0.2 mV s−1. b The rate performance of full cells with different electrolytes. c The voltage profiles of full cell assembled with aqueous gel electrolyte at different current densities. d Comparison of energy densities of various aqueous energy storage devices based on the total mass of the electrode active materials. Color code: cyan, brown, orange, blue, black, and violet represent Li−, Na−, K−, Mg−, Al−, Ca−based aqueous batteries, respectively. e The cycling stability of the full cells at 0.2 C. The mass ratio of Ca0.4MnO2 cathode to S@C anode is about 1.6: 1. f Water−soaking test of charged S@C|aqueous gel electrolyte|Ca0.4MnO2 pouch cell after corner−cut.

Supplementary Files

This is a list of supplementary files associated with this preprint. Click to download.

- SupplementaryInformation.docx
- SupplementaryVideo11mdissolution.mpg
- SupplementaryVideo28.37mdissolution.mpg
- SupplementaryVideo3Geldissolution.mpg
- SupplementaryVideo4Pouchcellcornercut.mp4